High performance carbon free bifunctional air electrode for advanced zinc-air batteries

Aroa R. Mainar [a,*], J. Alberto Blázquez [a,*], Domenico Frattini [b], Marina Enterría [b], Nagore Ortiz-Vitoriano [b,c], Idoia Urdampilleta [a], Hans-Jürgen Grande [a,d]

[a] CIDETEC, Basque Research and Technology Alliance (BRTA), P° Miramón, 196, Donostia-San Sebastián 20014, Spain
[b] Center for Cooperative Research on Alternative Energies (CIC energiGUNE), Basque Research and Technology Alliance (BRTA), Parque Tecnológico de Álava, Albert Einstein 48, Vitoria-Gasteiz 01510, Spain
[c] Ikerbasque, Basque Foundation for Science, María Díaz de Haro 3, Bilbao 48013, Spain
[d] Advanced Polymers and Materials, Physics, Chemistry and Technology Department, University of the Basque Country (UPV/EHU), Avda. Tolosa 72, Donostia-San Sebastián 20018, Spain

ABSTRACT

Secondary zinc-air batteries (ZABs) offer a promising alternative for the future of sustainable energy storage. However, the current capability of secondary ZABs is far from satisfactory. The limitations for achieving high reversibility are mainly related to the bifunctional air electrodes as it severely hampers practical applications and commercialization of secondary ZABs. Many efforts have been devoted to the development of efficient and corrosion resistant bifunctional electrocatalysts towards oxygen reduction reaction (ORR) and oxygen evolution reaction (OER). In ZABs, carbon is commonly used as conductive additive, however, it has been observed that carbon materials are not resistant to the high positive voltages applied in electrical recharge. In this work, the use of metallic nickel as alternative conductive additive in bifunctional air electrodes is explored and compared with carbon nanotubes (CNT). We demonstrate that the chemical resistance of CNT does not limit the electrode performance; but the density of the additive as well as its interaction with the active material is crucial for achieving long cycle life. The use of Ni as conductive agent in secondary ZABs boosted the cycle life by delivering more than 2,400 cycles, in contrast to the 88 cycles delivered by the analogous carbon-based battery.

1. Introduction

Rechargeable zinc-air batteries (ZABs) offer a promising alternative for the future of sustainable energy storage due to the high theoretical energy density, use of abundant and environmentally friendly materials and intrinsic safety. However, the limitations for achieving highly reversible ZABs are mainly related to the bifunctional air electrode (BAE) performance. Thus, achieving a durable catalyst with high efficiency in both oxygen reduction reaction (ORR) and oxygen evolution reaction (OER) reactions is a non-trivial issue [1,2].

The cathodic electrochemical reactions in ZABs are very complex because they occur in the three-phase interphase between the liquid (electrolyte), solid (catalyst) and gas (oxygen). As well, they involve multiple adsorption-desorption intermediates, reaction steps and, the formation of different products [3]. In this context, many efforts have been devoted to the development of efficient and corrosion resistant

bifunctional electrocatalysts towards ORR (discharge) and, OER (charge). Fig. 1 compares the publications related to catalysts for ZABs with the total publications in ZABs demonstrating that little attention has been paid to other cell materials. In that sense, relatively little attention has been paid to the stability of conductive additives used on BAE formulation, where carbon materials have commonly been used due to their, low cost, wide availability, optimal wettability, etc. [1]. Among them, BAEs containing carbon nanotubes (CNT) in their composition have demonstrated improved electrochemical performance [4–6]. For example, Zhang et al. [7] have very recently demonstrated that directly growing Mn-Co_3O_4 on CNT greatly improves the interaction between the catalyst and the conductive additive, resulting in longer cycling stability and lower voltage gap.

Unfortunately, it has been reported that carbon-based air electrodes are susceptible to rapid corrosion at the high oxidizing potentials during OER on a secondary ZAB. The formation of carbonate (CO_3^{2-}) ions from

* Corresponding authors.
E-mail addresses: aramos@cidetec.es (A.R. Mainar), ablazquez@cidetec.es (J.A. Blázquez).
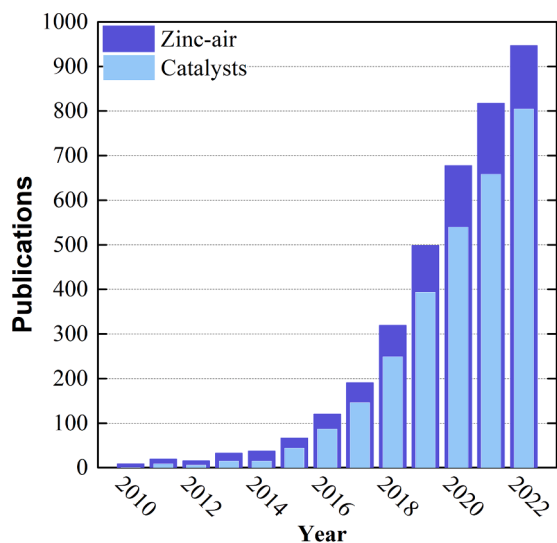
Fig. 1. Number of publications per year from 2010 to June 2022 mentioning the term "zinc-air-battery" or "zn-air battery" in the abstract, keywords or document title and including the term "catalyst" or "electrocatalyst" for publications about development of catalysts in ZAB. As derived from Scopus database (accessed on November 3, 2022).

carbon corrosion can combine with CO_2 poisoning from the outside atmosphere to hasten the precipitation of K_2CO_3 in the air electrode pores, which can block catalytic sites and limit the oxygen diffusion [8,9]. The formation of such carbonates decreases the triple phase boundary (TPB) active area, via excessive electrode flooding, impeding a free O_2 flow to the TPB, especially during discharge at high current densities, when a higher concentration of oxygen is needed [10,11]. The formation of decomposition products can cause the mechanical failure of the electrode [1,12].

In this context, metal-based air electrodes can offer much higher corrosion resistance than those containing carbon [8,13]. Silver and nickel have been reported as the main metal conductive additives employed for bifunctional air electrodes. Silver-based air electrodes have demonstrated increased stability in alkaline fuel cells and lithium-air batteries [14–16]. Alexander Kube et al. [17] reported the use of either Ni or Ag conductive additives within the electrodes for ZABs. Both showed corrosion effects after cycling being more severe for the silver-based electrode. Ni-based electrode retained its morphology and only showed pitting corrosion on its particles due to Kolbe-like decomposition reaction occurred due to the presence of potassium citrate in the electrolyte system. Moreover, nickel metal has been reported as low-cost, chemically stable, and promising additive material for air electrodes in rechargeable ZABs [8,10,18,19], while the high price of silver makes it impractical as conductive additive for low-cost ZABs [20]. In the present work, we compare the electrochemical performance of secondary ZABs using carbon and metal-based conductive additives in the air electrode formulation $NiCo_2O_4$ (NCO) was selected as bifunctional electrocatalyst since it is known to be an effective catalyst for both ORR and OER, showing small overpotentials compared to precious metals [8,18,19]. The physico-chemical properties of pristine materials and fresh/cycled electrodes were studied by Scanning Electron Microscopy (SEM), X-ray diffraction (XRD), N_2 physisorption, He pycnometry, and Raman spectroscopy. The electrochemical performance of the electrodes in a secondary ZAB based on aqueous alkaline electrolyte was evaluated in terms of power density, cell overpotential at different current densities, specific capacity, and reversibility. We demonstrate that the incorporation of carbon free electrodes increases the cyclability of the cell and stability of the electrode. Although the specific capacity does not change significantly, the power density, overpotential and reversibility are greatly improved by using nickel-based electrodes

(more than 27 times in the case of the reversibility). To understand such enhancement in the electrochemical performance by simply replacing the conductive additive from carbon material to nickel metal, additional postmortem analysis of cycled electrodes was performed.

2. Experimental methods

2.1. Preparation of secondary zinc-air battery electrolyte and electrodes

ZABs were assembled using a two-electrode configuration cell, comprising methacrylate cases and gaskets. They included an advanced aqueous alkaline electrolyte formulation, a zinc paste anode supported on a copper mesh (Copper Net Foil for Battery Anode Substrate, 55 μm, MTI Corporation) and a bifunctional air electrode. Both glass fiber filter (Whatman Grade GF/D, Whatman plc.) and Celgard® 5550 were used as separators.

The electrolyte formulation selected for this study has demonstrated to enhance the cycle life of rechargeable zinc-air batteries in previous works [21] and it consisted on ZnO (Sigma-Aldrich, 99% purity) saturated aqueous solution containing 7 M KOH (Sigma-Aldrich, 85% purity), 1.4 M KF (Sigma-Aldrich, 99% purity) and 1.4 M of K_2CO_3 (Sigma-Aldrich, 99% purity). ZnO, KF and K_2CO_3 were used as additives to reduce hydrogen evolution reaction (HER) and zinc dissolution through the electrolyte system [21–23].

A zinc paste was used as negative electrode, which was prepared by mixing 49.28 wt.% zinc powder (EverZinc), 21.12 wt.% zinc oxide (ZnO, EverZinc), 1.4 wt.% carboxymethyl cellulose (CMC, Cekol®) and 28.2 wt.% of the prepared electrolyte [21,24].

Two types of bifunctional air electrodes based either on carbon or metal additives were prepared: one containing carbon nanotubes (*viz.* c-BAE) and another containing nickel metal (*viz* m-BAE). Considering that CNT presents much higher volume and surface area than Ni, the catalyst loading was fixed to 24 mg_{NCO} cm^{-2} and, for a fair comparison, the volume/mass of the conductive additive was varied to achieve similar catalyst loading. c-BAE consisted of a mixture of 46 wt.% of CNT (Arkema Graphistrength™ C100) as conductive additive, 39 wt.% of NCO ($NiCo_2O_4$, CerPoTech) as bifunctional catalyst and 15 wt.% of PTFE (GoodFellow, 6-9 micron) as binder. On the other hand, m-BAE was based on a mixture of 70 wt.% of Ni (Strem Chemicals Inc., 3-7 μm) as conductive additive, 15 wt.% of NCO ($NiCo_2O_4$, CerPoTech) as bifunctional catalyst and 15 wt.% of PTFE (GoodFellow, 6-9 micron) as binder. These mixtures were pressed at 1 ton on a stainless-steel mesh (Haver & Boecker, AISI 304-L) for 2 min.

2.2. Electrochemical and physicochemical characterization

The electrochemical characterization was performed in a BaSyTec Cell Test System (Germany) at 25 ± 1°C controlled by air conditioning. The assembled batteries presented an open circuit voltage of 1.32 ± 0.02 V. The electrochemical performance was evaluated in terms of power density, cell overpotential at different current densities, specific capacity, and reversibility. The polarization data was collected by analyzing the galvanodynamic response of the zinc-air batteries based on c-BAE and m-BAE electrodes. Power densities were measured at 1 mA s^{-1} up to 0.5 V during 5 cycles [25]. Galvanostatic analyses were carried out for different current densities (1, 2, 3, 4, 5, 10 and 20 mA cm^{-2}) during 3 cycles for each current density. A total capacity of 35 mAh was extracted for each state of charge and discharge. After each current density, 1 mA cm^{-2} was applied in order to analyze the preservation of the BAE stability. The specific capacity of metallic zinc (mAh g_{Zn}^{-1}) was obtained over a full discharge at a constant current density of 2 mA cm^{-2} using 0.60 V as cut-off voltage. Finally, long-term reversibility test was performed at 2 mA cm^{-2} during 1 h in a voltage window from 2.2 V to 0.6 V for each charge and discharge state.

The physicochemical properties of raw materials comprising the electrode formulation and BAEs (either pristine and cycled) were stud-

ied by Scanning Electron Microscopy (SEM), X-ray diffraction (XRD), N_2 physisorption, He pycnometry, and Raman spectroscopy. The surface morphology of the materials was studied by a SEM microscope FEI Quanta250 (FEI Co., Hillsboro, OR, United States) operated at 5-10 kV under high-vacuum. The crystal structure of the BAE electrodes was determined via XRD with a D8 Advance diffractometer (Bruker co., Billerica, MA, United States) operated in the θ/2θ range of 10-80° (Cu Kα, λ= 1.5406 Å), a step size of 0.02° and a time per step of 0.482 s. An ASAP2020 adsorption analyser (Micromeritics, Norcross, GA, United States) was used to obtain the N_2 adsorption-desorption isotherms at –196°C in the relative pressure (P/P$_0$) range of 10^{-4} – 0.99. Samples were previously evacuated for 12 h at 200°C under vacuum. The specific surface area (S_{BET}) was calculated according to the Brunauer–Emmett–Teller (BET) method from the nitrogen isotherms in the relative pressure range of 0.05–0.25. The t-plot method was used to obtain the external surface area (S_{EXT}) in the relative pressure range of 0.07–0.25. The total volume of micro-mesopores (V_T) was calculated as the amount of N_2 adsorbed at a relative pressure of 0.99. Further textural analysis was conducted in an AccuPyc II 1340 pycnometer (Micromeritics, Norcross, GA, United States), to obtain the real density (ρ_r) and the total pore volume of micro, meso and macropores (V_P), which was calculated by the formula:

$$V_P = \frac{1}{\rho_a} - \frac{1}{\rho_r}$$

where ρ_a is the apparent density (g cm^{-3}) and ρ_r is the real density (g cm^{-3}).

Raman spectra were recorded in a shift range from 100 to 3200 cm^{-1} with a Renishaw spectrometer (Nanonics Multiview 2000) operating with an excitation wavelength of 532 nm, focused with a 50X long working distance objective. The spectra were obtained by performing 10 acquisitions with 10 s of exposure time of the laser beam to the sample. A surface mapping for each sample was acquired by measuring 10 different zones, thus ensuring a reliable evaluation of the phase composition. A silicon wafer was used for calibration. In the case of the postmortem analysis of cycled electrodes, all the samples were gently washed with distilled water (to remove the soluble deposits) and dried overnight prior to their analysis.

3. Results and discussion

The schematic fabrication procedure of bifunctional air electrodes and SEM images of raw materials and bifunctional air electrodes are shown in Fig. S1. The images show a porous morphology for c-BAE, compared to the compact/highly dense nature of m-BAE (Fig. S1 (e) *vs.* (f)). The SEM images of the pristine electrodes show three different phases *(i)* the particles of the binder (PTFE) embedded in the matrix of the BAE, *(ii)* fine particles probably belonging to NCO catalyst and *(iii)* the more abundant particles associated with the conductive additive, either CNT or Ni. Due to the different nature and morphology of the additives, c-BAE and m-BAE can be easily distinguished, *i.e.,* the one containing Ni is much denser. A higher density for nickel metal BAE is corroborated by analyzing the pores by gas physical adsorption. The isotherms and textural parameters for the two different BAEs are

displayed in Fig. S2 and Table 1, respectively.

It can be readily observed that m-BAE cathode does not present any porosity, at least in the micro-mesoporous range (the values for the textural parameters in Fig. S2 are almost negligible). In contrast, c-BAE presents an important mesoporosity and a specific surface area of 104 m^2 g^{-1}, where 94 cm^3 g^{-1} are meso-macropores (S_{ext}) and a total pore volume of 0.85 cm^3 g^{-1}.

To verify the existence of larger porosity in the electrodes, He pycnometry was conducted instead of Hg intrusion. The latter technique is commonly used for the study of meso-macropores but the high pressures applied to the sample can damage its structure, releasing uncertain results. Consistent with gas physisorption, the porosity calculated by He pycnometry is much larger for c-BAE compared with m-BAE, as it is shown in Table 1 (3.28 *vs.* 0.58 cm^3 g^{-1}). This, together with the larger density (both, apparent (ρ_a) and real (ρ_r)) of m-BAE, confirms that the electrode containing Ni as conductive agent is non-porous while the one having CNT is porous. Either the active material (NCO) or the binder (PTFE) does not present any porosity (Fig. S3 and Table S1). Therefore, the textural differences observed in the bifunctional electrodes are essentially caused by the different porosity and structure of Ni and CNT raw conductive additives (Fig. S3 and Table S1), that govern and impact the textural characteristics of the final BAE (Fig. S2 and Table 1).

The XRD patterns of the bifunctional air electrodes are shown in Fig. 2. For comparison, the patterns of raw materials are also included. c-BAE shows a peak ∼ 26°, which is related to CNT (card no. PDF-00-058-1638) [26,27], and other multiple peaks ascribed to the NCO catalyst (card no. PDF-00-020-0781) [28,29] (see Fig. 2(a). On the other hand, m-BAE shows a major contribution of Ni conductive additive (card no. PDF-01-071-4655) [8,30], where additional peaks related with NCO are also acknowledged in the inlet plot of Fig. 2(b). In general, the substantial overlapping of the patterns, without interaction, demonstrates the successful mixing of raw materials.

The electrochemical characterization of secondary zinc-air batteries based on c-BAE and m-BAE was performed at room temperature. The polarization curves were collected by galvanodynamic analysis during 5 cycles. Fig. 3(a) shows the power density curves for c-BAE and m-BAE at 1st and 5th cycle. During the first cycle, c-BAE presents higher power density than that obtained for m-BAE (48.71 mW cm^{-2} *vs.* 38.56 mW cm^{-2}, respectively). However, the electrochemical performance of c-BAE decreases as the cycle number increases and, m-BAE presents higher peak of power density in the 5th cycle (44.31 mW cm^{-2} *vs.* 36.31 mW cm^{-2}, respectively). The deterioration of the electrochemical performance of c-BAE during the battery operation could be related to the degradation of any of the components on the cathode formulation, as will be described later.

Fig. 3(b) shows the discharge profiles derived from the galvanodynamic analysis of the ZABs. c-BAE shows a voltage drop for which is also reflected in the shoulder in Fig. 3(a). This behaviour could be related to the inhomogeneous ZnO film deposition over the remaining metallic Zn as proposed by Stamm et al. [31]. In that sense, covered metallic zinc requires a jump in the driving force for oxidation, hence increasing the overpotential to overcome the passivation effect of the ZnO film, which is correlated to the mentioned voltage drop. A well optimized gas diffusion electrode guarantees stable oxygen concentrations through the cell and hence, the inhomogeneous ZnO deposition could be reduced.

At 1.0 V, the current density of c-BAE and m-BAE at the 5th cycle was 23.39 and 37.77 mA cm^{-2}, respectively, indicating an improved electrochemical performance of m-BAE with respect to c-BAE.

The cycling performance of secondary zinc-air battery at different current densities is shown in Fig. 4. The floating columns in Fig. 4(c) and (d) represent the overpotential at different current densities, where the maximum reflects the OER and the minimum the ORR.

The battery overpotential of c-BAE is lower than m-BAE for 1 and 2 mA cm^{-2} (Table S2) but it increases considerably for higher current densities (Fig. 4(a)). In contrast, the overpotential in m-BAE remain almost constant, regardless of the applied current (Fig. 4(b)). Solid blue
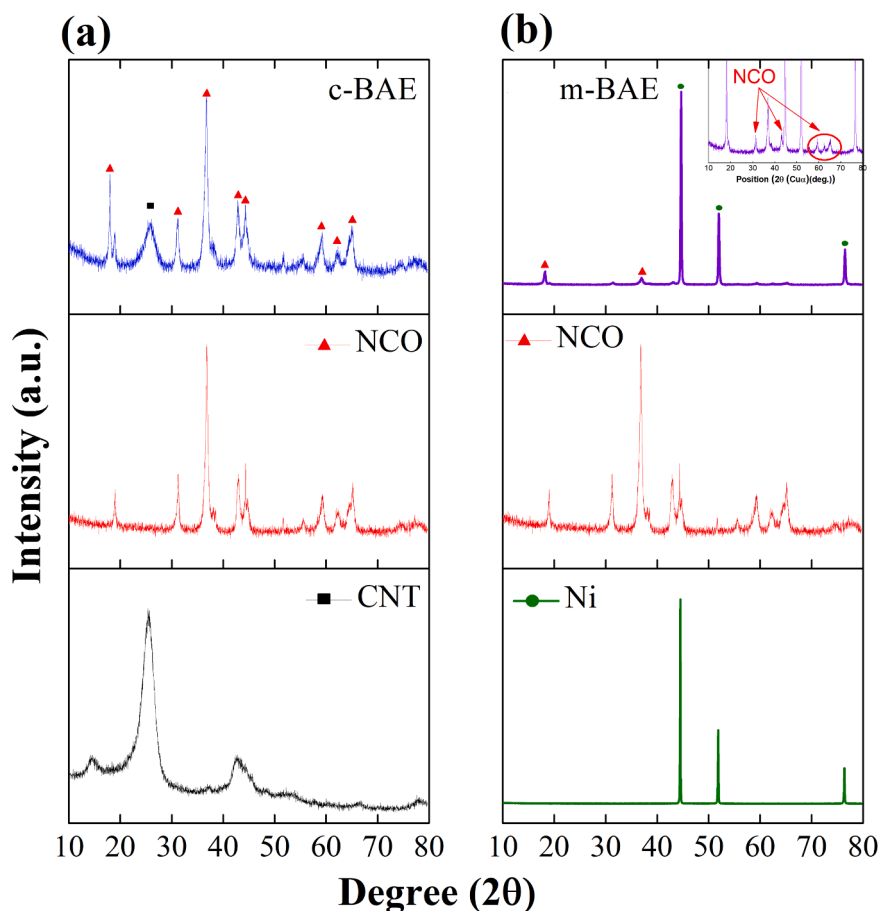
Table 1

Textural parameters obtained from N_2 adsorption–desorption isotherms in Fig. S2 at -196°C, and He pycnometry at room temperature of c-BAE and m-BAE.

		c-BAE	m-BAE
N_2 Physisorption	V_T (cm^3 g^{-1})	0.85	0.01
	S_{BET} (m^2 g^{-1})	104	2
	S_{EXT} (cm^3 g^{-1})	94	2
He pycnometry	ρ_a (g cm^{-3})	1.3	0.3
	ρ_r (g cm^{-3})	5.8	2.8
	V_P (cm^3 g^{-1})	3.28	0.58

Fig. 2. XRD patterns for (a) c-BAE and, (b) m-BAE including raw materials.
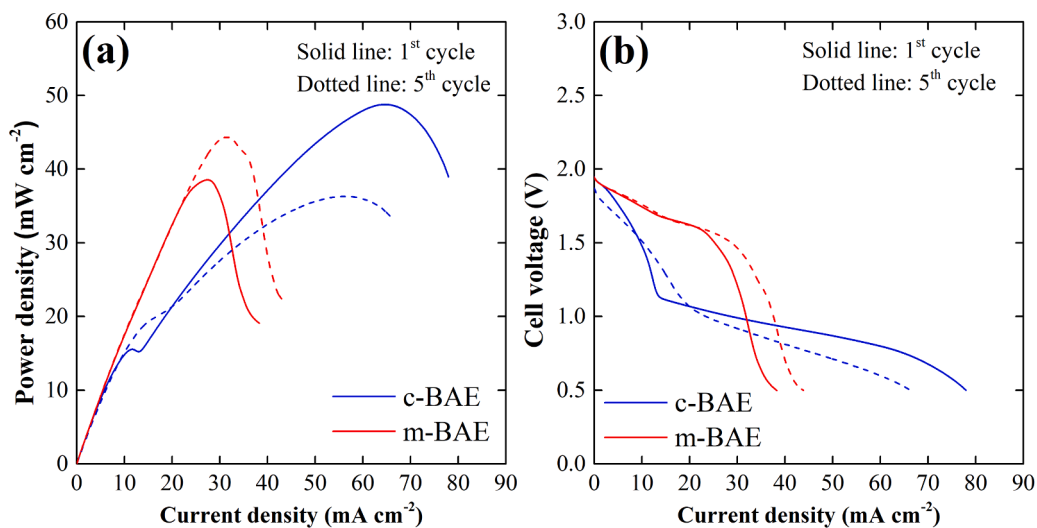

Fig. 3. (a) Power density of c-BAE and m-BAE (scan rate: 1 mA s^{-1}), and (b) discharge profiles of zinc-air batteries.

lines included in Fig. 4(c) and (d), represent the ORR and OER voltages at 1 mA cm^{-2} after applying the here proposed current densities. The ORR/OER potential at 1 mA cm^{-2} is preserved for m-BAE, even at high current densities Fig. 4(c). This is not the case of c-BAE electrode, which is not able to recover the ORR/OER voltages at 1 mA cm^{-2} and the overpotential increases gradually as the current intensity increases Fig. 4 (d). It can be therefore concluded that *i)* c-BAE based secondary zinc-air battery degrades as the current density increases and *ii)* m-BAE

electrode provide a stable cycling performance in a wide current range.

The discharge specific capacity at 2 mA cm^{-2} for the secondary zinc-air batteries assembled using c-BAE (778.53 mAh g$_{Zn}^{-1}$) and m-BAE (797.12 mAh g$_{Zn}^{-1}$) cathodes is very similar, as it is shown in Fig. 5(a). However, the coulombic efficiency of c-BAE based secondary zinc-air battery is much lower than m-BAE (51.37% *vs.* 94.72%). Regarding the specific energies, c-BAE delivers 290.38 Wh kg$_{cell}^{-1}$ while m-BAE based zinc-air battery delivers 242.99 Wh kg$_{cell}^{-1}$. The higher specific
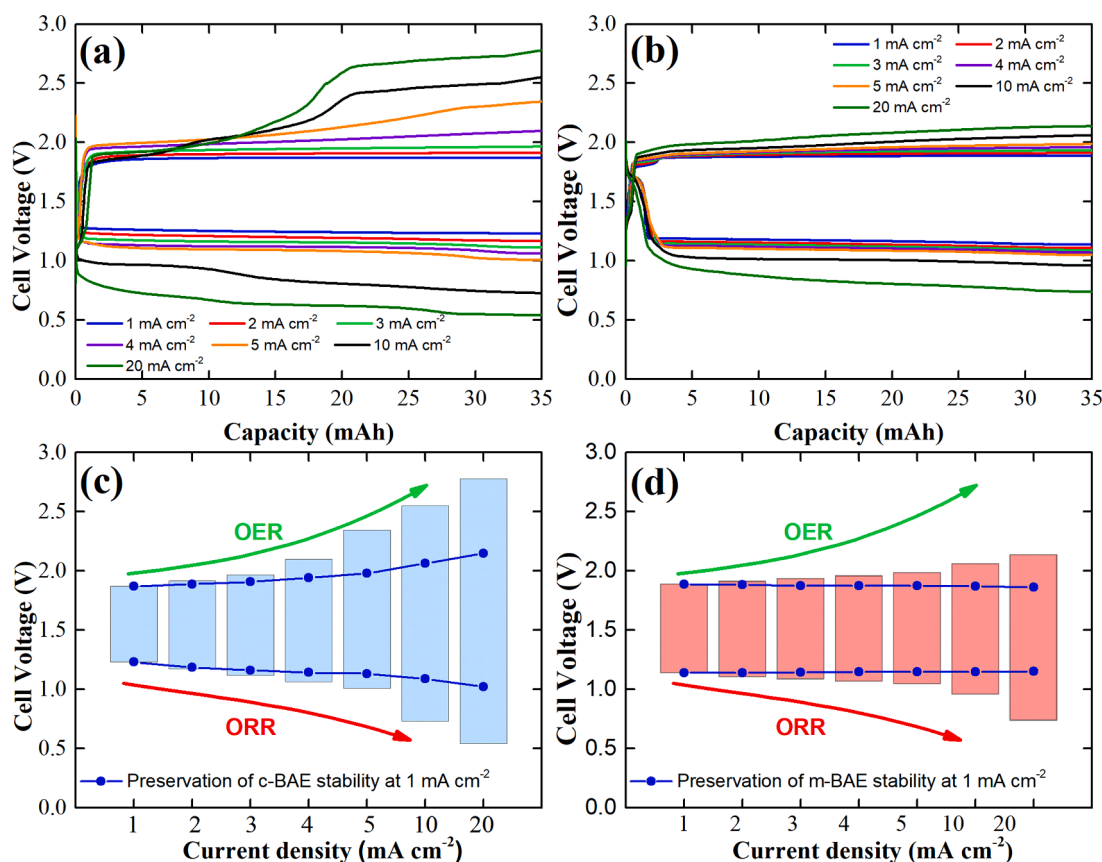
Fig. 4. Electrochemical profiles at 3rd cycle. (a) c-BAE and, (b) m-BAE. Maximum OER and ORR voltages at different current densities for (c) c-BAE and, (d) m-BAE. Solid blue line represents the ORR and OER voltage preservation at 1 mA cm^{-2} after applying different current densities.

energy of the c-BAE based secondary zinc-air battery is related to *(i)* the lighter weight of the carbon-based electrode and, *(ii)* the higher discharge voltage of the battery (see Fig. 5(a)).

The stability of secondary zinc-air batteries over the continuous charge and discharge cycling was evaluated by galvanostatic pulse cycling measurements, at a discharge and charge current density of 2 mA cm^{-2} for 1 hour per charge/discharge step. Fig. 5(b) shows that c-BAE was stable up to 88 cycles while the reversibility of m-BAE is higher than 2,400 cycles.

To understand huge difference between the electrochemical behavior c-BAE and m-BAE, postmortem analysis of the electrodes was conducted after the cyclability tests. The morphology of the cycled electrodes (Fig. 6(a) and (b)) was compared with that in pristine ones (Fig. S1) by SEM imaging. Compared to the pristine, cycled c-BAE shows less particle agglomerates (compare Figs. 6(a) and S1 (e)) while m-BAE shows some small pits and fractures (compare Figs. 6(b) and S1 (f)).

The chemical/crystalline nature of cycled electrodes was also investigated by XRD in Fig. 6(c) and (d). Compared to pristine, cycled electrodes show additional phases, probably caused by the formation of several parasitic products during battery cycling. For both c-BAE and m-BAE, the characteristic peaks of the raw materials present in the electrode formulation; *i.e.* conductive additives CNT (around 26°, card no. PDF-00-058-1638) and Ni (around 44°, card no. PDF-01-071-4655), PTFE binder (around 18°, card no. PDF-00-047-2217) and NCO catalyst (around 18° and 37°, card no. PDF-00-020-0781) are still visible in the postmortem analysis. In the case of c-BAE, these peaks have smaller intensity than in pristine electrode, due to the interference and overlapping of the other phases formed during cycling. The phases crystallizing on c-BAE during cycling are ascribed to anhydrous KOH (card no. PDF-00-015-0890), K$_2$CO$_3$ (card no. PDF-00-016-0820) and hydrocarbonate KHCO$_3$ (minor phase, card no. PDF-01-070-0997). On the

contrary, the XRD spectrum of m-BAE is very similar to that obtained for pristine electrode.

The pristine and cycled BAEs were also studied by Raman spectroscopy (Fig. 7). A surface mapping for each sample was acquired by measuring 10 different zones to discard inhomogeneities on the surface composition. The different raw materials existing in the electrode formulation were also studied and their spectra were represented at the bottom of Fig. 7 to unequivocally identify their signals. CNT, NCO, and PTFE displayed a clear pattern while Ni metal had no signal in Raman spectroscopy. Pristine c-BAE and m-BAE display the peaks corresponding to the raw materials present on each formulation. The collected spectra seem to be more reproducible for pristine m-BAE (Fig. 7(b)), indicating a more homogeneous mixture for this electrode. The use of complementary characterization techniques in postmortem analysis is highly recommended as the detection of side products or the observation of structural changes in the electrode surface is not always straightforward. For instance, the quantitative detection limits for carbonates in powder XRD are higher than those in Raman and, consistently, the presence of carbonates in cycled c-BAE was not observed in Fig. 7(b). After cycling, c-BAE displays the peaks corresponding to CNT nanotubes while the signal of the NCO active material is negligible or inexistent (Fig. 7(a)). In contrast, the cycled m-BAE maintains the signals for NCO indicating a better stability of the active material when using Ni metal as additive (Fig. 7(b)). It can be therefore concluded that metals (Ni) can be a better additive for metal oxides (NCO) due to a stronger interaction between the two phases, thus inhibiting the leaching of the active material while cycling. This is not the case of c-BAE, where the interaction of NCO with CNT might be weaker, and the active material is dissolved in the alkaline electrolyte during cycling. On the other hand, the bands related to CNT additive in c-BAE did not show any modification (nor intensity or shift) from pristine electrode to that cycled (Fig. S4),
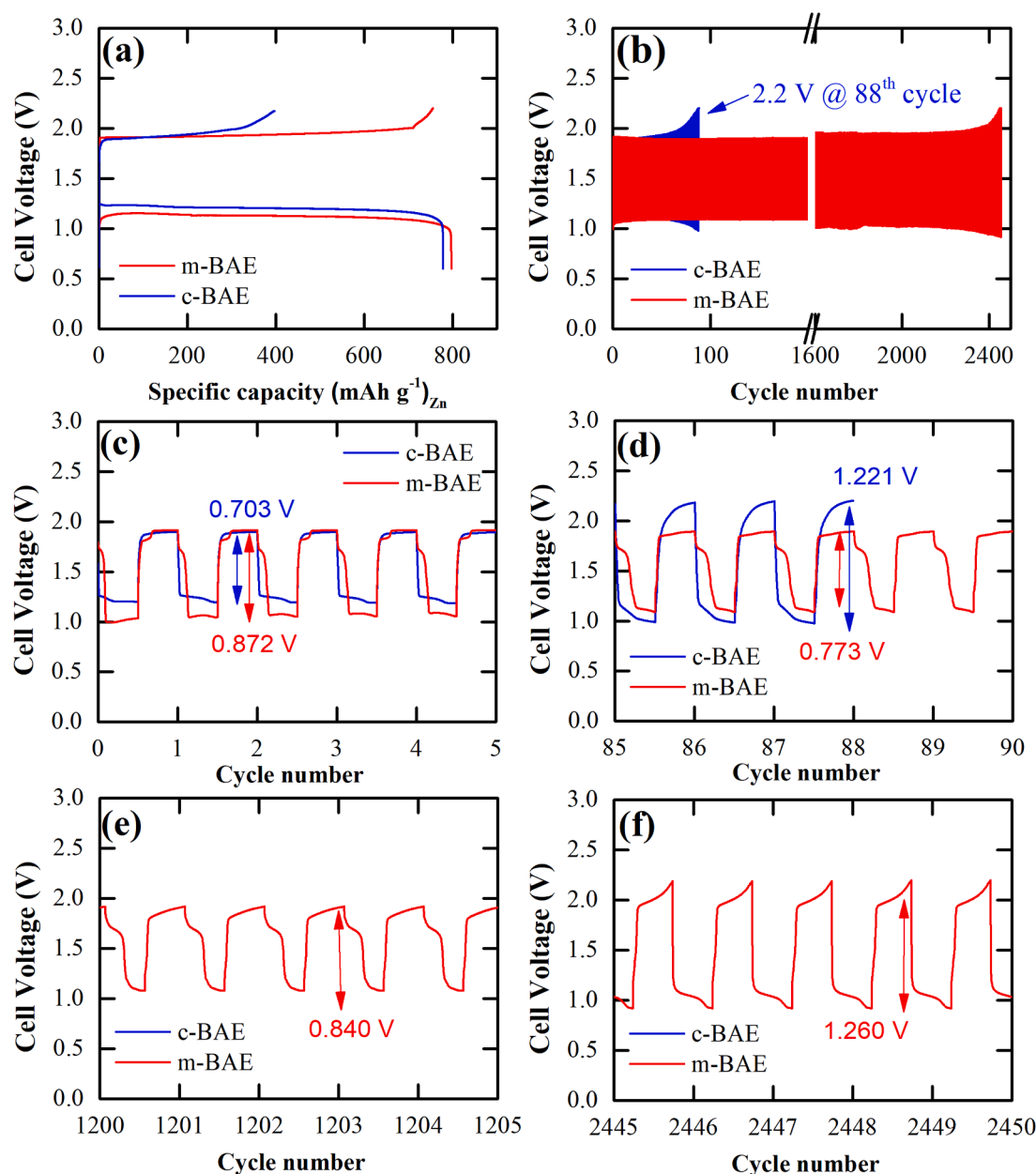
Fig. 5. (a) Full discharge curve at 2 mA cm^{-2}, (b) reversibility of c-BAE and m-BAE at 2 mA cm^{-2} and, (c-f) charge/discharge profiles at different cycling stage (c) 0-5, (d) 85-90, (e) 1200-1205, and (f) 2445-2450 cycles.

indicating that the carbon-based additive does not undergo oxidation (at least significant) during charge. Hence, the carbonates observed on the surface of cycled c-BAE by XRD (Fig. 6(c)) must come from any process different from carbon oxidation. The porous nature of CNT could enhance the CO_2 permeation from air, in contrast to the dense structure of Ni metal, leading to the formation of carbonates as side products. The significant difference in the electrochemical performance of c-BAE and m-BAE cathodes (power and energy density, cycle life, stability…) can be therefore ascribed to two different phenomena; *(i)* the formation of carbonates promoted by the porous structure of CNT additive and *(ii)* the loss of active material during cycling caused by a weak interaction between the metal oxide and carbon materials. Hence, the NCO active material dissolution is observed for the c-BAE, after 88 cycles, and not for m-BAE, after 2,400 cycles in both XRD (Fig. 6) and Raman (Fig. 7) analysis.

Finally, a comparison with the relevant literature is proposed in Table 2. Liquid electrolyte ZABs, using NCO-based or Co/Ni-based active

materials have been considered, together with cathode formulations using carbon materials as conductive additives (physically mixed) or as support (the active material was directly grown on the carbon surface). For fair comparison, works using cycling conditions (*i.e.*, current density and time per cycle) similar to those in this work were included. It can be observed that when NCO and carbon materials are used in the cathode, and the ZAB cycled at 2 mA cm^{-2}, several hundreds of cycles are usually achieved. Using very short cycle times has the effect to increase the number of cycles but considering a real application, the storage/usage time is too short to demonstrate an appealing competitiveness with other electrochemical storage technologies. For example, when the time per cycle is increased to 1 h, ZABs using NCO and carbon-based materials show a smaller number of cycles [32,33], and the same occurs if the applied current density is increased, even for short cycle times [28,34]. The c-BAE tested in this work confirms this finding, and also benchmarks that BAEs with carbon materials hardly achieve hundred cycles for time per cycle > 1-2 h. On the contrary, when non-carbon materials are used,
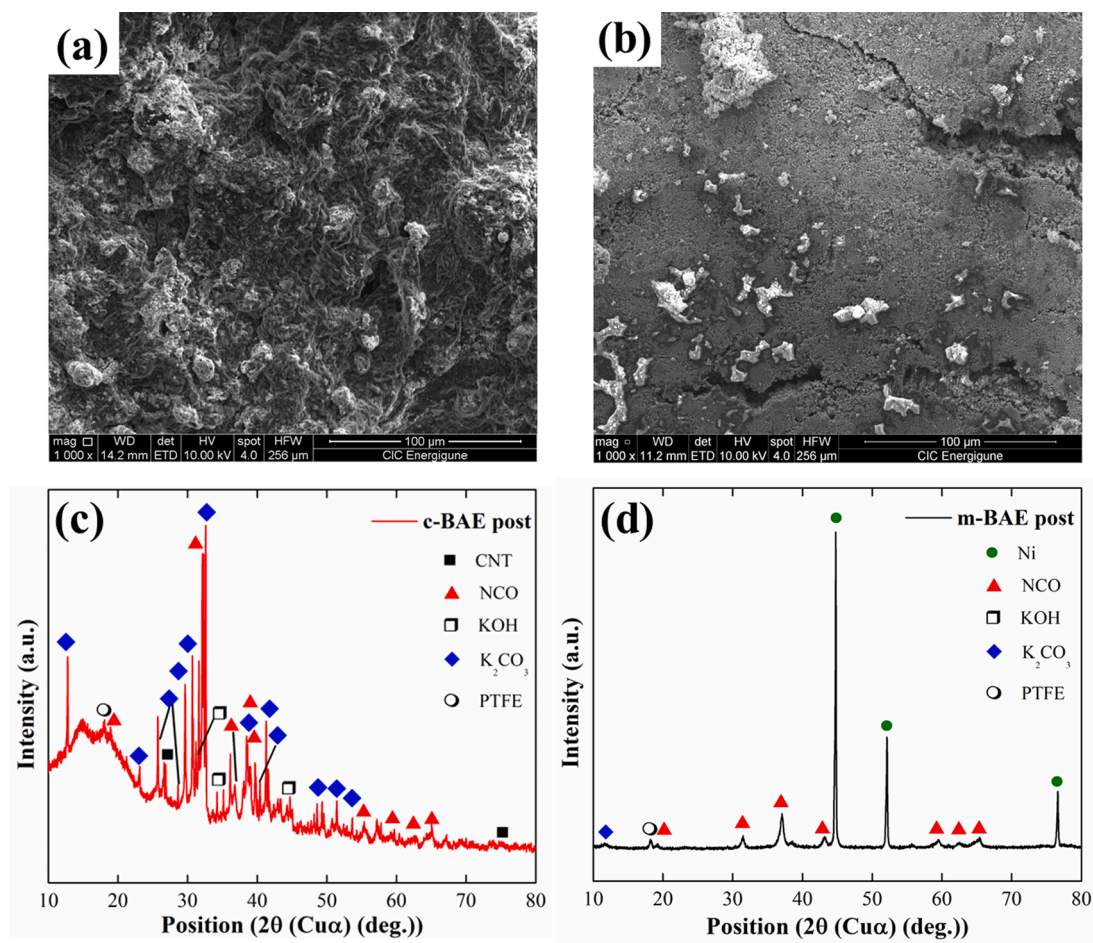
Fig. 6. SEM images after cyclability tests for (a) c-BAE and (b) m-BAE. Postmortem XRD analysis for (c) c-BAE and (d) m-BAE.
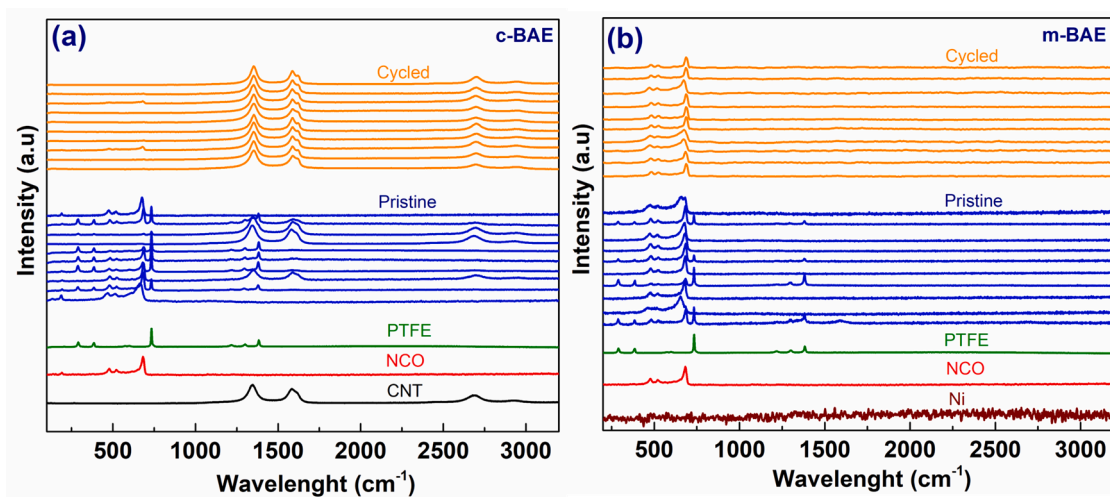

Fig. 7. 10 zones Raman mapping for pristine and cycled (a) c-BAE and (b) m-BAE electrodes. The Raman spectra of the raw materials in each electrode formulation are displayed at the bottom of the figures for an easy identification of the signals of each component.

e.g., Ni foam [35,36], for short cycle times higher current densities can be applied, and a notable number of cycles is obtained, but an extensive comparison and more reference works are needed. The brief comparison reported in Table 2 shows that the m-BAE developed in this work is able to guarantee a notable number of cycles, higher than those stated in literature, for long cycles (2 h) compared to the very short cycles (10, 20, 30 min) usually reported, thus representing a benchmark for the field. It

can be concluded that the use of Ni metal as conductive additive in NCO cathodes is scarcely reported whereas carbon-based supports/additives represent the standard, and discharge/charge times are limited to the minute scale in many cases, and just few works report cycles longer than 1 h. Therefore, the performance achievable by applying longer cycle times and higher current densities must be further explored. Moreover, this remarkable result is due to the different interaction/integration of

Table 2
Comparison of cycling performance of recent carbon support/additive-based BAEs vs. the m-BAE developed in this work.

BAE active material	Support	Conductive additive	Current density (mA cm^{-2})	Discharge/charge time (h)	N. of cycles (-)	Refs.
CoNi	N-CNT-NP	-	2	0.083/0.083	540	[37]
CoP/NiFeP	N-doped Carbon	-	2	0.333/0.333	300	[38]
CoFe	N-doped Ketjen black	-	2	0.083/0.083	600	[39]
NCO@NiMn LDH	Ni foam	-	20	0.083/0.083	500	[35]
NCO hollow nanofibers	-	-	2	0.5/0.5	30	[32]
Mn$_{0.5}$Ni$_{0.5}$Co$_2$O$_4$		Vulcan carbon	10	0.07/0.07	150	[34]
NCO nanowire	-	-	20	0.33/0.33	50	[28]
NCO	C-coated Ni foam	-	5	0.25/0.25	5,200	[36]
NCO nanowhiskers	Pyrolyzed porous carbon	Activated carbon+ acetylene black	10	0.167/0.167	1,460	[40]
NCO/Mo$_2$C	Carbon cloth	-	10	0.5/0.5	300	[41]
Co(OH)$_2$/NCO	N-doped rGO	-	2	0.5/0.5	180	[33]
NCO	NiCo/N-doped CNTs	-	2	1.0/1.0	293	[42]
NCO	N-doped graphene	XC-72 Vulcan carbon	10	0.083/0.083	540	[43]
NCO	N-doped GO	Activated carbon	5 mA mg^{-1}	0.083/0.083	>75	[44]
NCO nanoplates	-	XC-72 Vulcan carbon	5	0.167/0.167	50	[45]
NCO nanosheets	-	Activated carbon	10	0.167/0.167	225	[46]
NCO	-	CNT	2	1.0/1.0	88	**This work**
NCO	-	Ni metal	2	1.0/1.0	>2,400	**This work**

the active material with the conductive additive, suggesting that the same material (*i.e.*, NCO) can be better exploited by changing and optimizing the selection of the additives, giving more durable and stable BAEs. This is an important advance to assess the cyclability and durability of BAE in secondary aqueous ZABs for the future penetration of the technology in the market.

4. Conclusions

In this work, carbon free (m-BAE) and carbon based (c-BAE) electrodes have been studied as air bifunctional cathodes in ZABs. For that purpose, the loading of the NiCo$_2$O$_4$ catalyst on the electrode has been fixed and either CNT or Ni have been evaluated as conductive additives. We demonstrated that both the porosity and the chemical nature of additive plays a crucial role in the performance of the battery. Thus, the metal-based cathode presents higher power density and long-term durability comparing with the cell containing carbon additive (more than 27 times higher; 2450 *vs.* 88 cycles). A postmortem study of the cycled samples revealed that such divergent electrochemical behavior is related to a higher stability of the metal-based electrode where the loss of NCO active material by leaching is prevented by a strong metal-metal oxide interaction. Additionally, the compact/non-porous structure of nickel hinders the permeation of CO$_2$ from atmosphere and limits the formation of carbonate by product.

Comparing to previous works of NCO based ZABs, herein developed m-BAE presents higher reversibility even evaluating the reversibility for longer cycles (2 h *vs.* 10, 20, 30 min used in the literature). This suggests that the active material can be better exploited by changing and optimizing the conductive additives. Moreover, more works dealing with different cycling conditions (higher current density, longer cycle times) are needed to further benchmark the profitable benefits of Ni- or other metal-based conductive additives in BAE of ZABs demonstrated in this work.

CRediT authorship contribution statement

Aroa R. Mainar: Conceptualization, Validation, Formal analysis, Investigation, Writing – original draft, Writing – review & editing, Visualization, Supervision, Project administration, Funding acquisition. **J. Alberto Blázquez:** Conceptualization, Formal analysis, Writing – review & editing, Visualization, Supervision, Project administration, Funding acquisition. **Domenico Frattini:** Conceptualization, Validation, Formal analysis, Investigation, Writing – review & editing, Visualization, Supervision, Project administration, Funding acquisition. **Marina Enterría:** Conceptualization, Validation, Formal analysis, Investigation, Writing – review & editing, Visualization, Supervision, Project administration, Funding acquisition. **Nagore Ortiz-Vitoriano:** Conceptualization, Validation, Formal analysis, Investigation, Writing – review & editing, Visualization, Supervision, Project administration, Funding acquisition. **Idoia Urdampilleta:** Conceptualization. **Hans-Jürgen Grande:** Conceptualization.

Declaration of Competing Interest

The authors declare that they have no known competing financial interests or personal relationships that could have appeared to influence the work reported in this paper.

Data availability

No data was used for the research described in the article.

Acknowledgements

Supplementary materials

Supplementary material associated with this article can be found, in the online version, at doi:10.1016/j.electacta.2023.142075.

References

[1] S. Velraj, J.H. Zhu, Cycle life limit of carbon-based electrodes for rechargeable metal–air battery application, J. Electroanal. Chem. 736 (2015) 76–82, https://doi.org/10.1016/j.jelechem.2014.11.003.

[2] M. Mechili, C. Vaitsis, N. Argirusis, P.K. Pandis, G. Sourkouni, C. Argirusis, Research progress in transition metal oxide based bifunctional electrocatalysts for aqueous electrically rechargeable zinc-air batteries, Renew. Sustain. Energy Rev. 156 (2022), 111970, https://doi.org/10.1016/j.rser.2021.111970.

[3] L. Jörissen, Bifunctional oxygen/air electrodes, J. Power Sources 155 (2006) 23–32, https://doi.org/10.1016/j.jpowsour.2005.07.038.

[4] X. Xiao, X. Li, J. Wang, G. Yan, Z. Wang, H. Guo, Y. Liu, Robust assembly of urchin-like NiCo$_2$O$_4$/CNTs architecture as bifunctional electrocatalyst in Zn-Air batteries, Ceram. Int. 46 (2020) 6262–6269, https://doi.org/10.1016/j.ceramint.2019.11.096.

[5] P.C. Li, C.C. Hu, T.H. You, P.Y. Chen, Development and characterization of bi-functional air electrodes for rechargeable zinc-air batteries: effects of carbons, Carbon N. Y. 111 (2017) 813–821, https://doi.org/10.1016/j.carbon.2016.10.057.

[6] Z. Zhao, W. Yu, W. Shang, Y. He, Y. Ma, Z. Zhang, P. Tan, Revealing the effects of conductive carbon materials on the cycling stability of rechargeable Zn-air batteries, Int. J. Energy Res. 46 (2022) 7694–7703, https://doi.org/10.1002/er.7669.

[7] X. Zhang, Q. Liu, S. Liu, E. Wang, Manganese-doped cobalt spinel oxide as bifunctional oxygen electrocatalyst toward high-stable rechargeable Zn-air battery, Electrochim. Acta 437 (2023), 141477, https://doi.org/10.1016/j.electacta.2022.141477.

[8] Z.P. Cano, M.G. Park, D.U. Lee, J. Fu, H. Liu, M. Fowler, Z. Chen, New interpretation of the performance of nickel-based air electrodes for rechargeable zinc–air batteries, J. Phys. Chem. C 122 (2018) 20153–20166, https://doi.org/10.1021/acs.jpcc.8b06243.

[9] T. Wang, M. Kunimoto, T. Mori, M. Yanagisawa, J. Niikura, I. Takahashi, M. Morita, T. Abe, T. Homma, Carbonate formation on carbon electrode in rechargeable zinc-air battery revealed by in-situ Raman measurements, J. Power Sources 533 (2022), 231237, https://doi.org/10.1016/j.jpowsour.2022.231237.

[10] N. Borchers, S. Clark, B. Horstmann, K. Jayasayee, M. Juel, P. Stevens, Innovative zinc-based batteries, J. Power Sources 484 (2021), 229309, https://doi.org/10.1016/j.jpowsour.2020.229309.

[11] X. Cai, L. Lai, J. Lin, Z. Shen, Recent advances in air electrodes for Zn–air batteries: electrocatalysis and structural design, Mater. Horiz. 4 (2017) 945–976, https://doi.org/10.1039/C7MH00358G.

[12] S. Velraj, A.K. Estes, B.L. Bates, J.H. Zhu, Effects of testing conditions on the performance of carbon-supported bifunctional electrodes, Electrochim. Acta 292 (2018) 446–457, https://doi.org/10.1016/j.electacta.2018.09.168.

[13] J. Fu, Z.P. Cano, M.G. Park, A. Yu, M. Fowler, Z. Chen, *Electrically rechargeable zinc-air batteries: progress, challenges, and perspectives*, Adv. Mater. 29 (2017), 1604685, https://doi.org/10.1002/adma.201604685.

[14] E. Gülzow, N. Wagner, M. Schulze, Preparation of gas diffusion electrodes with silver catalysts for alkaline fuel cells, Fuel Cells 3 (2003) 67–72, https://doi.org/10.1002/fuce.200320221.

[15] F. Bidault, A. Kucernak, A novel cathode for alkaline fuel cells based on a porous silver membrane, J. Power Sources 195 (2010) 2549–2556, https://doi.org/10.1016/j.jpowsour.2009.10.098.

[16] D. Wittmaier, N. Wagner, K.A. Friedrich, H.M.A. Amin, H. Baltruschat, Modified carbon-free silver electrodes for the use as cathodes in lithium–air batteries with an aqueous alkaline electrolyte, J. Power Sources 265 (2014) 299–308, https://doi.org/10.1016/j.jpowsour.2014.04.142.

[17] A. Kube, N. Wagner, K.A. Friedrich, Influence of organic additives for zinc-air batteries on cathode stability and performance, J. Electrochem. Soc. 168 (2021), 050531, https://doi.org/10.1149/1945-7111/abff63.

[18] X. Li, D. Pletcher, A.E. Russell, F.C. Walsh, R.G.A. Wills, S.F. Gorman, S.W.T. Price, S.J. Thompson, A novel bifunctional oxygen GDE for alkaline secondary batteries, Electrochem. Commun. 34 (2013) 228–230, https://doi.org/10.1016/j.elecom.2013.06.020.

[19] S.W.T. Price, S.J. Thompson, X. Li, S.F. Gorman, D. Pletcher, A.E. Russell, F.C. Walsh, R.G.A. Wills, The fabrication of a bifunctional oxygen electrode without carbon components for alkaline secondary batteries, J. Power Sources 259 (2014) 43–49, https://doi.org/10.1016/j.jpowsour.2014.02.058.

[20] A.R. Mainar, E. Iruin, J.A. Blázquez, High performance secondary zinc-air/silver hybrid battery, J. Energy Storage 33 (2021), 102103, https://doi.org/10.1016/j.est.2020.102103.

[21] A.R. Mainar, E. Iruin, L.C. Colmenares, J.A. Blázquez, H.J. Grande, Systematic cycle life assessment of a secondary Zinc–air battery as a function of the alkaline electrolyte composition, Energy Sci. Eng. 6 (2018), https://doi.org/10.1002/ese3.191.

[22] A.R. Mainar, O. Leonet, M. Bengoechea, I. Boyano, I. de Meatza, A. Kvasha, A. Guerfi, J.Alberto Blázquez, Alkaline aqueous electrolytes for secondary zinc-air batteries: an overview, Int. J. Energy Res. 40 (2016) 1032–1049, https://doi.org/10.1002/er.3499.

[23] A.R. Mainar, E. Iruin, L.C. Colmenares, A. Kvasha, I. de Meatza, M. Bengoechea, O. Leonet, I. Boyano, Z. Zhang, J.A. Blazquez, An overview of progress in electrolytes for secondary zinc-air batteries and other storage systems based on zinc, J. Energy Storage 15 (2018) 304–328, https://doi.org/10.1016/j.est.2017.12.004.

[24] A.R. Mainar, L.C. Colmenares, J.A. Blázquez, I. Urdampilleta, A brief overview of secondary zinc anode development: The key of improving zinc-based energy storage systems, Int. J. Energy Res. 42 (2018) 903–918, https://doi.org/10.1002/er.3822.

[25] P. Tan, B. Chen, H. Xu, W. Cai, W. He, H. Zhang, M. Liu, Z. Shao, M. Ni, Integration of Zn–Ag and Zn–air batteries: a hybrid battery with the advantages of both, ACS Appl. Mater. Interfaces 10 (2018) 36873–36881, https://doi.org/10.1021/acsami.8b10778.

[26] E. Iruin, A.R. Mainar, M. Enterría, N. Ortiz-Vitoriano, J.A. Blázquez, L.C. Colmenares, T. Rojo, S. Clark, B. Horstmann, Designing a manganese oxide bifunctional air electrode for aqueous chloride-based electrolytes in secondary zinc-air batteries, Electrochim. Acta 320 (2019), 134557, https://doi.org/10.1016/j.electacta.2019.134557.

[27] M.L. Chen, W.C. Oh, Synthesis and highly visible-induced photocatalytic activity of CNT-CdSe composite for methylene blue solution, Nanosc. Res. Lett. 6 (2011) 398, https://doi.org/10.1186/1556-276X-6-398.

[28] M. Prabu, K. Ketpang, S. Shanmugam, Hierarchical nanostructured NiCo$_2$O$_4$ as an efficient bifunctional non-precious metal catalyst for rechargeable zinc–air batteries, Nanoscale 6 (2014) 3173, https://doi.org/10.1039/c3nr05835b.

[29] Y. Zhai, H. Mao, P. Liu, X. Ren, L. Xu, Y. Qian, Facile fabrication of hierarchical porous rose-like NiCo$_2$O$_4$nanoflake/MnCo$_2$O$_4$nanoparticle composites with enhanced electrochemical performance for energy storage, J. Mater. Chem. A Mater. 3 (2015) 16142–16149, https://doi.org/10.1039/C5TA03017J.

[30] S. Ahmed, J. Shim, H.-J. Sun, H.-R. Rim, H.-K. Lee, G. Park, Nickel decorated bimetallic catalysts derived from metal-organic frameworks as cathode materials for rechargeable Zinc-Air batteries, Mater. Lett. 283 (2021), 128781, https://doi.org/10.1016/j.matlet.2020.128781.

[31] J. Stamm, A. Varzi, A. Latz, B. Horstmann, Modeling nucleation and growth of zinc oxide during discharge of primary zinc-air batteries, J. Power Sources 360 (2017) 136–149, https://doi.org/10.1016/j.jpowsour.2017.05.073.

[32] C. Tomon, S. Sarawutanukul, N. Phattharasupakun, S. Duangdangchote, P. Chomkhuntod, P. Kidkhunthod, M. Sawangphruk, Insight into photoelectrocatalytic mechanisms of bifunctional cobaltite hollow-nanofibers towards oxygen evolution and oxygen reduction reactions for high-energy zinc-air batteries, Electrochim. Acta 392 (2021), 139022, https://doi.org/10.1016/j.electacta.2021.139022.

[33] X. Peng, J. Zhang, T. Cen, Z. Ye, Y. Liu, D. Yuan, Co(OH)$_2$-NiCo$_2$O$_4$ hybrid nanosheets coupled with N-doping reduced graphene oxide as efficient electrocatalysts for Zn-air batteries, J. Alloys Compd. 872 (2021), 159441, https://doi.org/10.1016/j.jallcom.2021.159441.

[34] J. Béjar, L. Álvarez–Contreras, F. Espinosa–Magaña, J. Ledesma–García, N. Arjona, L.G. Arriaga, Zn–air battery operated with a 3DOM trimetallic spinel (Mn$_{0.5}$Ni$_{0.5}$Co$_2$O$_4$) as the oxygen electrode, Electrochim. Acta 391 (2021), 138900, https://doi.org/10.1016/j.electacta.2021.138900.

[35] X. Guo, T. Zheng, G. Ji, N. Hu, C. Xu, Y. Zhang, Core/shell design of efficient electrocatalysts based on NiCo$_2$O$_4$nanowires and NiMn LDH nanosheets for rechargeable zinc–air batteries, J. Mater. Chem. A Mater. 6 (2018) 10243–10252, https://doi.org/10.1039/C8TA02608D.

[36] B. Li, J. Quan, A. Loh, J. Chai, Y. Chen, C. Tan, X. Ge, T.S.A. Hor, Z. Liu, H. Zhang, Y. Zong, A robust hybrid Zn-battery with ultralong cycle life, Nano Lett. 17 (2017) 156–163, https://doi.org/10.1021/acs.nanolett.6b03691.

[37] J. Li, Y. Wang, Z. Yin, R. He, Y. Wang, J. Qiao, In-situ growth of CoNi bimetal anchored on carbon nanoparticle/nanotube hybrid for boosting rechargeable Zn-air battery, J. Energy Chem. 66 (2022) 348–355, https://doi.org/10.1016/j.jechem.2021.08.007.

[38] E. Vijayakumar, S. Ramakrishnan, C. Sathiskumar, D.J. Yoo, J. Balamurugan, H.S. Noh, D. Kwon, Y.H. Kim, H. Lee, MOF-derived CoP-nitrogen-doped carbon@NiFeP nanoflakes as an efficient and durable electrocatalyst with multiple catalytically active sites for OER, HER, ORR and rechargeable zinc-air batteries, Chem. Eng. J. 428 (2022) 131115, https://doi.org/10.1016/j.cej.2021.131115.

[39] S. Ren, X. Duan, F. Ge, Z. Chen, Q. Yang, M. Zhang, H. Zheng, Novel MOF-derived hollow CoFe alloy coupled with N-doped Ketjen Black as boosted bifunctional oxygen catalysts for Zn–air batteries, Chem. Eng. J. 427 (2022), 131614, https://doi.org/10.1016/j.cej.2021.131614.

[40] X. Xiao, X. Hu, Y. Liang, G. Zhang, X. Wang, Y. Yan, X. Li, G. Yan, J. Wang, Anchoring NiCo$_2$O$_4$ nanowhiskers in biomass-derived porous carbon as superior oxygen electrocatalyst for rechargeable Zn-air battery, J. Power Sources 476 (2020), 228684, https://doi.org/10.1016/j.jpowsour.2020.228684.

[41] C. Xu, Q. Wang, S. Zhao, S. Wang, NiCo$_2$O$_4$ nanoneedle/Mo2C-coated carbon cloth as efficient catalyst for water splitting and metal-air battery, Synth. Met. 280 (2021), 116894, https://doi.org/10.1016/j.synthmet.2021.116894.

[42] C. Chen, H. Su, L.-N. Lu, Y.-S. Hong, Y. Chen, K. Xiao, T. Ouyang, Y. Qin, Z.-Q. Liu, Interfacing spinel NiCo$_2$O$_4$ and NiCo alloy derived N-doped carbon nanotubes for enhanced oxygen electrocatalysis, Chem. Eng. J. 408 (2021), 127814, https://doi.org/10.1016/j.cej.2020.127814.

[43] Y. Ma, W. Shang, W. Yu, X. Chen, W. Xia, C. Wang, P. Tan, Synthesis of Ultrasmall NiCo$_2$O$_4$nanoparticle-decorated n-doped graphene nanosheets as an effective catalyst for Zn–Air batteries, Energy Fuels 35 (2021) 14188–14196, https://doi.org/10.1021/acs.energyfuels.1c02064.

[44] P. Moni, S. Hyun, A. Vignesh, S. Shanmugam, Chrysanthemum flower-like NiCo$_2$O$_4$–nitrogen doped graphene oxide composite: an efficient electrocatalyst for

lithium–oxygen and zinc–air batteries, Chem. Commun. 53 (2017) 7836–7839, https://doi.org/10.1039/C7CC03826G.

[45] P. Tan, Z. Wu, B. Chen, H. Xu, W. Cai, S. Jin, Z. Shao, M. Ni, Cation-substitution-tuned oxygen electrocatalyst of spinel cobaltite MCo_2O_4(M = Fe, Co, and Ni) hexagonal nanoplates for rechargeable Zn-air batteries, J. Electrochem. Soc. 166 (2019) A3448–A3455, https://doi.org/10.1149/2.1311914jes.

[46] J. Zhao, Y. He, Z. Chen, X. Zheng, X. Han, D. Rao, C. Zhong, W. Hu, Y. Deng, Engineering the surface metal active sites of nickel cobalt oxide nanoplates toward enhanced oxygen electrocatalysis for Zn–air battery, ACS Appl. Mater. Interfaces 11 (2019) 4915–4921, https://doi.org/10.1021/acsami.8b16473.